PHYSICAL REVIEW FLUIDS **9**, 054003 (2024)

Editors' Suggestion

Exit dynamics of a sphere launched underneath a liquid bath surface

Xiaofeng Wei,[1] Dege Li,[2] Jing Lei,[1] Jinglu Li,[1] Javier Rivero-Rodríguez,[3] Fangye Lin,[4,*] Dongyun Wang,[1,†] and Benoit Scheid[5]

[1]*College of Engineering, Zhejiang Normal University, 321004 Jinhua, China*
[2]*School of Mechanical and Power Engineering, Nanjing Tech University, 211816 Nanjing, China*
[3]*Escuela Técnica Superior de Ingenieros Industriales, Universidad de Málaga, 29013 Málaga, Spain*
[4]*Ningbo Innovation Center, Zhejiang University, Ningbo 315100, China*
[5]*TIPs–Fluid Physics Unit, Université Libre de Bruxelles C.P. 165/67, 1050 Brussels, Belgium*

(Received 27 February 2024; accepted 12 April 2024; published 17 May 2024)

In this paper, we investigate the exit dynamics of a sphere launched underneath a liquid bath surface at a prescribed impact velocity. Spheres with radii approximate or smaller than the capillary length are considered. Following our previous work of a ligament drawn of a liquid bath [J. Fluid Mech. **922**, A14 (2021)], a two-dimensional model is applied to describe the liquid dynamics, and the whole exit dynamics up to the descent or the pinch-off moments is considered. The process can be sequenced into a partial exit stage that forms a coated layer and a full exit stage with an attached ligament. A bouncing-off regime, a lower pinch-off penetration regime, and an upper pinch-off penetration regime are identified, separating by a penetration Weber number and a switching Weber number. The phase diagram is revealed, where the two critical Weber numbers are functions of the Bond number. By considering the energy evolutions, we show that the impact energy is mainly converted into the surface energy and the gravitational potential energy for the low- and large-gravity cases, respectively. The coated layer is mainly formed in the partial exit stage, whose maximum volume increases with the impact velocity but decreases with gravity effect. Stretching motion is shown to have negligible influence on the local pinch-off behavior, while it determines the appearance and the location of pinch-off. Our results can help to understand the exit behaviors of aquatic animals, and the design of microamphibious aircraft or energy collection devices.

DOI: 10.1103/PhysRevFluids.9.054003

I. INTRODUCTION

The exit of an object from liquid into air is a common phenomenon in everyday life experience, e.g., animals jumping out of water [1–3], the water exit of a ping-pong ball [4], and bubble rising and burst in a bottle [5–7]. Various industrial applications can be found associated with the exit motion, such as the liquid film processing [8], the stereolithographic printing [9], food processing [10], the water exit of an amphibious aircraft [11], and the energy collection of wave energy devices [12]. In process of films pulled out of a pure liquid bath using a horizontal fiber [8], understanding the exit dynamics could help to predict the coating thickness and consequently the thickness of the entrained film.

The process can be modelled by a sphere launched below a liquid bath surface at a certain initial velocity whose dynamics mainly depends on the radius and the impact velocity. The flow

*Corresponding author: linfy@zju.edu.cn
†Corresponding author: zsdwdy@zjnu.edu.cn

 ©2024 American Physical Society

is mainly turbulent for large objects in a water bath, such as frogs and fishes with sizes much larger than the capillary length, where inertial and gravitational forces dominate the dynamics. Takamure and Uchiyama [13–15] studied the influence of the launch depth by controlling the impact velocity onto the air-water interface; they found that the maximum exit height decreases with larger launch depth due to the energy loss caused by the asymmetry of the interface, while results converge when the launch depth is deep enough. This independent depth has also been investigated for spheres, cylinders, and axisymmetric bodies either launched with constant velocities or with constant accelerations [16–18], the values of which are in the range of 3 to 10 times the radius. Truscott *et al.* [4] studied the water exit of buoyant spheres. They found that increasing the release depth does not always increase the pop-up height, and the dynamics is related to the submerged trajectory, which depends on the sphere density and the Reynolds number. Ni and Wu [19] showed that a more slender shape could foster the exit dynamics. On the other hand, the exit dynamics of small objects with sizes below the capillary length has received less attention [1,8]. Gravity is negligible in these cases with large Froude numbers, and the flow mainly turns to be laminar. Two regimes have been identified [1], namely the bouncing-off regime and the penetration regime, and the critical impact velocity is found to increase with the object size. However, due to the complexity of the interface motion, the exit dynamics remains unclear heretofore. We therefore focus on the exit dynamics of small objects, and the first objective of this work is to determine the critical impact velocity for penetration.

Before the sphere reaches the interface, it first deforms the interface. By considering the inviscid liquid and neglecting the surface tension, the analytical solution of free-surface elevation has been studied for more than a century [20–22]. The interface deformation is determined by the impact velocity. Telste [18] reported that the flow for the slow approach behaves essentially the same as the approach to a rigid wall, while the interface deforms like an interior boundary in an infinite fluid for the fast approach, and wave oscillation is evident for intermediate approach velocities. The interface deformation is found to play a key role on drainage dynamics during the approaching of a bubble towards the interface [6]. Liju *et al.* [16] reported experiments of axisymmetric objects approaching a free surface at a constant velocity, and they showed that for small or slow approaching objects, viscous forces significantly modify the liquid drainage above the dome and hence the free surface profile. The interface above the object later develops into a coated layer, which is related to the classical drag-out problem [23–25]. The coating thickness on a fiber obeys the well-known Landau-Levich-Derjaguin theory for slow pulling with negligible inertia effects, and hence increases with the velocity, whereas it is associated to the presence of a boundary layer for fast pulling with significant inertia effects, and hence decreases with the velocity [24]. The second objective then is to investigate the evolution of the coating layer and determine the corresponding entrained coated volume.

After the sphere rises above the bath, a ligament is formed between the sphere and the liquid bath, which obstructs the upward motion of the object. The ligament contracts radially during the rising phase and breaks when the impact velocity is large enough. The breakup is intrinsically due to Rayleigh-Plateau instability, leading to a characteristic timescale that mainly depends on the ligament radius for low-viscosity liquids [26]. It has been reported that the breakup time decreases with the increasing of axial stretching velocities or accelerations [27–30]. We have recently showed that the breakup of stretched ligaments are determined by the competition between contractions sequentially dominated by ductility and capillarity [31]. For ligament under fast stretching, the attached ligament could be quite long and could break into many droplets [32,33]. The breakup of ligament ends up with pinch-off when the local dynamics dominates. Another phenomenon that can be observed is the switch of the pinch-off location. Various works show that slow stretching induces the lower pinch-off, while fast stretching induces the upper pinch-off due to the strong upward suction effect [29,34,35]. The third objective of this work is to study the evolution of the ligament and the pinch-off dynamics.

In this paper we present a nonstationary two-dimensional model to describe the exit dynamics of a sphere launched underneath a liquid bath surface. This paper will be organized in the following

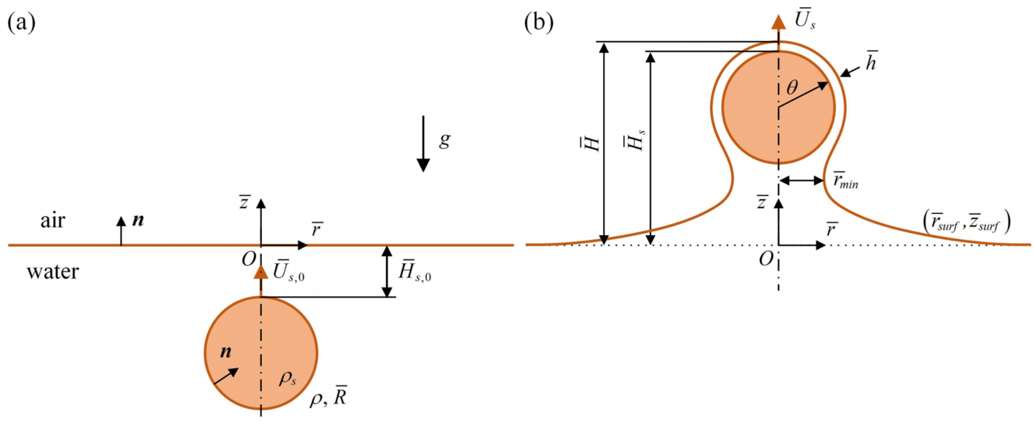

FIG. 1. Sketches of the sphere and the liquid bath under consideration. The initial configuration is presented in (a) and at a later time in (b) (see text for details). The dotted line in (b) represents the initially flat surface of the bath.

sequence. The two-dimensional model is presented in Sec. II. Typical results and the dynamic regimes are introduced in Sec. III. The energy evolutions, the coating dynamics, and the pinch-off dynamics are discussed in Sec. IV. Finally the conclusions are given in Sec. V.

II. MATHEMATICAL MODEL AND NUMERICAL METHOD

A. Problem settings

We consider a sphere launched underneath a water bath surface at a prescribed velocity. The physicochemical parameters of water considered are density $\rho = 1000\ \mathrm{kg\,m^{-3}}$, dynamic viscosity $\mu = 1$ mPa s, and surface tension $\gamma = 0.072\ \mathrm{N\,m^{-1}}$. As shown in Fig. 1, a cylindrical coordinate system is built for the system, whose center is vertically located at the initial flat interface and coaxial with the sphere. A neutrally buoyant sphere of radius $\bar{R}$ and density $\rho_s = \rho$ is initially located at $\bar{z} = \bar{H}_{s,0} < 0$ in the water bath and launched at a velocity $\bar{U}_{s,0}$ upwards. Note that the bar denotes a dimensional variable. The flow field and the interface shape are assumed to be axisymmetric with respect to the $\bar{z}$ axis. The typical later dynamic configuration is shown in Fig. 1(b), with a coated layer and an attached ligament. The transient sphere position and velocity are respectively $\bar{H}_s(\bar{t})$ and $\bar{U}_s(\bar{t})$, the interface top position is $\bar{H}(\bar{t})$, the minimum radius of the ligament is $\bar{r}_{\min}(\bar{t})$, the interface position is at $(\bar{r}_{\mathrm{surf}}, \bar{z}_{\mathrm{surf}})$, and the thickness of the coated layer is $\bar{h}(\theta, \bar{t})$, where θ represents the angle relative to the positive $\bar{z}$ axis and the angle vertex is at the center of the sphere.

The flow in the water bath can be modelled with the continuity and the momentum equations

$$\bar{\nabla} \cdot \bar{\boldsymbol{v}} = 0, \tag{1a}$$

$$\rho(\partial_{\bar{t}}\bar{\boldsymbol{v}} + \bar{\boldsymbol{v}} \cdot \bar{\nabla}\bar{\boldsymbol{v}}) = \bar{\nabla} \cdot \bar{\boldsymbol{\sigma}} - \rho g \boldsymbol{e}_z, \tag{1b}$$

where $\bar{\boldsymbol{\sigma}} = -\bar{p}\boldsymbol{I} + \mu[\bar{\nabla}\bar{\boldsymbol{v}} + (\bar{\nabla}\bar{\boldsymbol{v}})^T]$ is the stress tensor, $\bar{p}$ the pressure, $\bar{\boldsymbol{v}} = \bar{v}_z\boldsymbol{e}_z + \bar{v}_r\boldsymbol{e}_r$ the velocity, and $g = 9.8\ \mathrm{m\,s^{-2}}$ the gravitational acceleration. Note that $\boldsymbol{n} = n_z\boldsymbol{e}_z + n_r\boldsymbol{e}_r$ is the outer unit normal vector of the calculation domain, as shown in Fig. 1(a). The vertical forces are considered in this paper, i.e., the gravitational force and the resistive force, which can be written respectively as

$$\bar{G} = -\frac{4}{3}\pi\rho\bar{R}^3 g, \quad \bar{F} = -2\pi\left(\int_{\Sigma_s} \bar{\boldsymbol{\sigma}} \cdot \boldsymbol{n}\bar{r}d\bar{l}\right) \cdot \boldsymbol{e}_z, \tag{2}$$

where Σ_s is the sphere boundary and $d\bar{l}$ represents the axisymmetric contour element. The acceleration and the transient velocity then are respectively

$$\bar{a}_s(\bar{t}) = \frac{3(\bar{G}+\bar{F})}{4\pi\rho\bar{R}^3}, \quad \bar{U}_s(\bar{t}) = \bar{U}_{s,0} + \int_0^{\bar{t}} \bar{a}_s(\bar{t}')d\bar{t}'. \tag{3}$$

B. Nondimensionalized problem

Using the following transformations:

$$\bar{z} \to \bar{R}z, \quad \bar{r} \to \bar{R}r, \quad \bar{\nabla} \to \frac{1}{\bar{R}}\nabla, \quad \bar{t} \to \bar{\tau}t, \quad \bar{\boldsymbol{v}} \to \frac{\bar{R}}{\bar{\tau}}\boldsymbol{v}, \quad \bar{a}_s \to \frac{\bar{R}}{\bar{\tau}^2}a_s,$$
$$\bar{p} \to \frac{\gamma}{\bar{R}}p, \quad \bar{\boldsymbol{\sigma}} \to \frac{\gamma}{\bar{R}}\boldsymbol{\sigma}, \quad \bar{F} \to \gamma\bar{R}F, \quad \bar{G} \to \gamma\bar{R}G, \tag{4}$$

where $\bar{\tau} = \sqrt{\rho\bar{R}^3/\gamma}$ is the capillary timescale, the nondimensional system of equations becomes

$$\nabla\cdot\boldsymbol{v} = 0, \tag{5a}$$

$$(\partial_t\boldsymbol{v} + \boldsymbol{v}\cdot\nabla\boldsymbol{v}) = \nabla\cdot\boldsymbol{\sigma} - \mathrm{Bo}\boldsymbol{e}_z, \tag{5b}$$

where $\boldsymbol{\sigma} = -p\boldsymbol{I} + \mathrm{Oh}[\nabla\boldsymbol{v} + (\nabla\boldsymbol{v})^T]$ is the dimensionless stress tensor, $\mathrm{Oh} = \mu/\sqrt{\rho\gamma\bar{R}}$ is the Ohnesorge number, and $\mathrm{Bo} = \rho g\bar{R}^2/\gamma$ is the Bond number. The dimensionless forces then are

$$G = -\frac{4}{3}\pi\mathrm{Bo}, \quad F = -2\pi\left(\int_{\Sigma_s}\boldsymbol{\sigma}\cdot\boldsymbol{n}rdl\right)\cdot\boldsymbol{e}_z. \tag{6}$$

The dimensionless acceleration and transient velocity are respectively

$$a_s(t) = \frac{3(G+F)}{4\pi}, \quad U_s(t) = \sqrt{\mathrm{We}} + \int_0^t a_s(t')dt', \tag{7}$$

where $\mathrm{We} = \rho\bar{U}_{s,0}^2\bar{R}/\gamma$ the launch Weber number. All variables discussed are nondimensionalized henceforth.

C. Initial and boundary conditions

In the axisymmetric configuration, the space- and time-dependent variables are the pressure p, the axial velocity v_z, and the radial velocity v_r. The initial dimensionless position of the sphere is $H_s(0) = H_{s,0}$, which determines the initial calculation domain. The boundary of the calculation domain Ω consists of the following components. The free surface Σ_{surf}, applied with the kinematic condition and the dynamic condition,

$$\boldsymbol{v}_s\cdot\boldsymbol{n} = \boldsymbol{v}\cdot\boldsymbol{n}, \quad \text{and } \boldsymbol{\sigma}\cdot\boldsymbol{n} = \kappa\boldsymbol{n}, \tag{8}$$

where $\boldsymbol{v}_s$ is the velocity at the interface, $\kappa = -\nabla_s\cdot\boldsymbol{n}$ is the curvature, and $\nabla_s = (\boldsymbol{I} - \boldsymbol{nn})\cdot\nabla$ is the surface gradient operator. The no-slip condition applies at the surface of the sphere Σ_s,

$$v_z = U_s(t) \text{ and } v_r = 0, \tag{9}$$

the symmetry condition applies at the axisymmetric boundary Σ_{axi} at $r = 0$,

$$\partial_r v_z = 0, \quad \text{and } v_r = 0, \tag{10}$$

and the hydrostatic condition applies at the bottom boundary Σ_{bot} and the outside boundary Σ_{out},

$$\boldsymbol{\sigma}\cdot\boldsymbol{n} = \mathrm{Bo}\,z\boldsymbol{n}. \tag{11}$$

As initial guess, the liquid is assumed at rest,

$$p|_{t=0} = -\mathrm{Bo}z, \quad v_z|_{t=0} = 0, \quad v_r|_{t=0} = 0, \tag{12}$$

but because of the instantaneous launch of the sphere at speed $U_{s,0}$, the velocity field is iterated first to satisfy all boundary conditions at $t = 0$.

D. Numerical method

The above system holds in the deformable axisymmetric domain $\Omega(t)$ with both radial and axial dimensionless sizes L_b, occupied by water at time $t = 0$. For the moving mesh, we use an arbitrary Lagrangian-Eulerian formulation with a specific mesh treatment at the boundary [36]. In this method, the domain $\boldsymbol{x}(\boldsymbol{X}, t) \in \Omega(t)$ is parameterized by the initial position $\boldsymbol{X} = \boldsymbol{x}(\boldsymbol{X}, 0) \in \Omega(0)$, defining a time-dependent displacement field, $\boldsymbol{q} = \boldsymbol{x} - \boldsymbol{X}$, which satisfies

$$\nabla^2 \boldsymbol{q} = 0 \ \text{ at } \ \Omega. \tag{13}$$

The initial condition for the displacement is

$$\boldsymbol{q}|_{t=0} = \boldsymbol{0} \ \text{ at } \ \Omega. \tag{14}$$

We use a Eulerian description for the velocity of the free surface, the displacement of the sphere, the axisymmetric boundary, the fixed bottom, and the fixed side boundary, respectively, expressed as

$$\begin{gathered} \partial_t \boldsymbol{q} = v_n \boldsymbol{n} \quad \text{at } \ \Sigma_{\text{surf}}, \quad \boldsymbol{q} = \int_0^t U_s(t')dt'\boldsymbol{e}_z \quad \text{at } \ \Sigma_s, \\ \boldsymbol{q} \cdot \boldsymbol{n} = 0 \quad \text{at } \ \Sigma_{\text{axi}}, \quad \boldsymbol{q} = \boldsymbol{0} \quad \text{at } \ \Sigma_{\text{bot}} \ \text{ and } \ \Sigma_{\text{out}}, \end{gathered} \tag{15}$$

where $v_n = \boldsymbol{v} \cdot \boldsymbol{n}$. The system of Eqs. (5)–(7) and (13), supplemented by the initial conditions (12) and (14), and the boundary conditions (8)–(11) and (15) are solved in COMSOL 5.4, coupled with the weak form PDE and the moving mesh modules. Linear Lagrangian interpolants are used for the pressure and quadratic ones for the velocity and displacement. The bath size L_b is chosen large enough to have no influence on the dynamics. The quality of the mesh is ensured by remeshing when the distortion exceeds a certain value, and the independence of the results with respect to the mesh and remeshing criteria has been checked. The simulations are stopped when $H_s < H_{s,0}$ in the case of bouncing or $r_{\min} = 10^{-2}$ in the case of pinch-off (see details in Sec. IV C). Model validation is presented in Appendix A.

E. Launched underneath the interface

It is known that the launch position below the bath influences the exit dynamics. Takamure and Uchiyama [13,14] reported experiments of spheres launched at different initial positions while controlling the impact velocity to be the same, where the impact velocity $U_{s,\text{im}}$ is defined as the transient sphere velocity at $H_s = 0$. They found that when the launch depth increases, more liquid will be entrained out of the bath, which later develops into droplets scattered around the sphere. For deep launch with $H_{s,0} \leqslant -6$, Takamure and Uchiyama [13,14] showed that the result converges, namely it only depends on the impact velocity and is independent of the launch depth. In Appendix B, we show numerically that the result also converges for $H_{s,0} \geqslant -3$, which is named as the underneath launch.

In this paper, we focus on the exit dynamics of the underneath launch. To control the impact velocity more conveniently, we choose the launch position as $H_{s,0} = -0.1$, note $U_{s,\text{im}} \approx U_{s,0}$ when $H_{s,0} = -0.1$, details are presented in Appendix B. The launched velocity $U_{s,0}$ and the launched Weber number We are therefore mentioned as the impact velocity and the impact Weber number henceforth, respectively. Based on the above, it results that the problem is governed by two independent parameters, the Bond number and the impact Weber number. The following parameter space is considered in the present paper:

$$10^{-3} \leqslant \text{Bo} \leqslant 10, \quad 1 \leqslant \text{We} \leqslant 40. \tag{16}$$

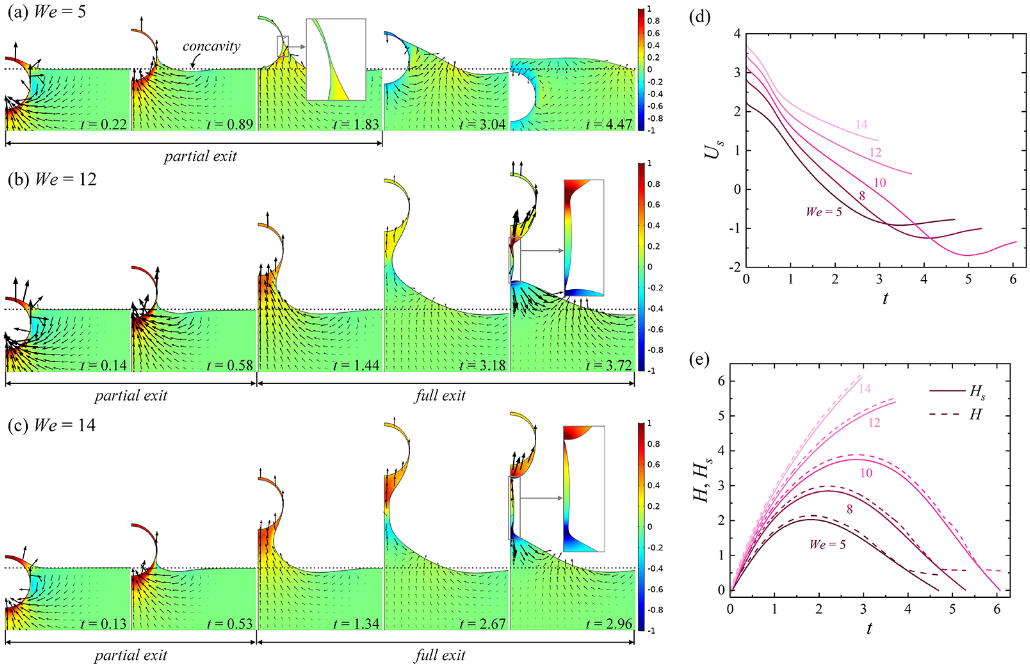

FIG. 2. [(a)–(c)] Velocity vectors for impact Weber numbers We $= 5, 12, 14$, with Bond number Bo $= 0.1$. The partial and full exit stages are marked out respectively for $H \leqslant 2$ and $H > 2$, the color represents the axial velocity, and the dotted line indicates the initial flat bath surface. (d) The transient sphere velocity U_s and (e) the transient sphere position H_s and the interface top position H for different impact Weber numbers We $= 5, 8, 10, 12, 14$, with Bond number Bo $= 0.1$.

Note that, since the liquid considered is water, the Ohnesorge number and the Reynolds number (defined as $\mathrm{Re} = \rho \bar{U}_{s,0}\bar{R}/\mu$) can be expressed as a function of Bo. The Ohnesorge number is $\mathrm{Oh} = \mathrm{Oh}_{\ell_c}\mathrm{Bo}^{-1/4}$, and the Reynolds number is $\mathrm{Re} = \mathrm{We}^{1/2}\mathrm{Bo}^{1/4}/\mathrm{Oh}_{\ell_c}$, respectively, in the range of $0.0013 \leqslant \mathrm{Oh} \leqslant 0.013$ and $79 \leqslant \mathrm{Re} \leqslant 4970$, where $\mathrm{Oh}_{\ell_c} = \mu/\sqrt{\rho\gamma\ell_c} = 0.0023$ is the Ohnesorge number for the capillary length $\ell_c = \sqrt{\gamma/\rho g}$. The Froude number (defined as $\mathrm{Fr} = \bar{U}_{s,0}/\sqrt{g\bar{R}}$), representing ratio of inertia to gravity, can be expressed as $\mathrm{Fr} = \mathrm{We}^{1/2}/\mathrm{Bo}^{1/2}$ and is in the range of $0.32 \leqslant \mathrm{Fr} \leqslant 200$.

III. RESULTS

A. Typical results

For various impact Weber numbers We and Bond numbers Bo, three regimes can be identified for the dynamics: (i) the bouncing-off regime, for which pinch-off never appears or appears during the descending phase; (ii) the lower pinch-off penetration regime, for which pinch-off appears at the lower part of the ligament during the rising phase; and (iii) the upper pinch-off penetration regime, for which pinch-off appears at the upper part of the ligament during the rising phase. By penetration, we mean that the sphere keeps moving upwards after it detaches from the bath. Cases with pinch-off during the descending phase thus belong to the bouncing-off regime. Typical cases are shown in Fig. 2, with the velocity field in Fig. 2(a)–2(c), the transient sphere velocity in Fig. 2(d), the transient sphere position and the interface top position in Fig. 2(e). The exit process can be divided into a partial exit stage for $H \leqslant 2$ and a full exit stage for $H > 2$. For slow launch with We $= 5$, the sphere stays in the partial exit stage, as presented in Fig. 2(a). Since the liquid is displaced by the rising sphere, the interface above the sphere is elevated and a concave deformation

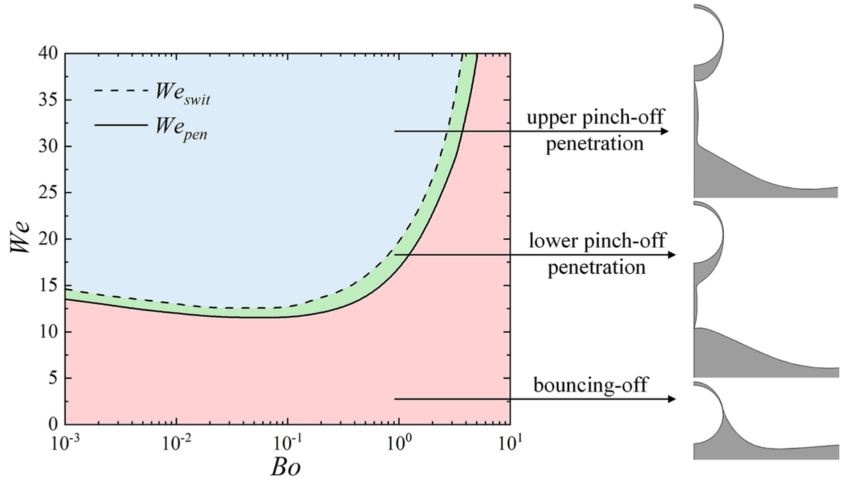

FIG. 3. The penetration Weber number $\mathrm{We}_{\mathrm{pen}}$ and the switching Weber number $\mathrm{We}_{\mathrm{swit}}$, varying with the Bond number Bo. The sketches at the maximum height for the three regimes are presented on the right.

is formed around the sphere, which have been found experimentally [1,15] and analytically [20,21]. As the sphere rises, the elevated interface deforms along the sphere and forms a coated layer, whose thickness is relatively large at the top and can be quite thin around the equator, as shown in the inset of Fig. 2(a) at $t = 1.83$. Under the action of gravitational and capillary forces, the sphere gradually slows down and reaches a maximum height $H_s \approx 2$ at $t = 1.83$, then descends back towards the bath with $U_s < 0$, as presented in Figs. 2(d) and 2(e). For faster launch with $\mathrm{We} = 8, 10$, the sphere goes higher and enters the full exit stage for $H > 2$ and then descends to the bath, as presented in Figs. 2(d) and 2(e). For these cases, pinch-off does not occur during the rising phase, which corresponds to the bouncing-off regime.

When the impact velocity is larger, e.g., $\mathrm{We} = 12,\ 14$ in Figs. 2(b) and 2(c), pinch-off occurs during the rising phase. In the full exit stage, an attached ligament is formed and stretched by the rising sphere. Note that, in this paper, the ligament is defined as the liquid between the sphere and the bath when $H > 2$, namely it only occurs in the full exit stage. For the trigger of the capillary instability [31], the competition between instability and stretching can be observed in the velocity field. As presented in Fig. 2(b) for $\mathrm{We} = 12$, the liquid in the ligament flows upwards at $t = 1.44$, indicating the dominant role of stretching, while it is propelled out of the ligament both upward and downward at $t = 3.18$, indicating the dominant role of capillary instability. The ligament then finally ends up with pinch-off at the position close to the bath for $\mathrm{We} = 12$ [see inset of Fig. 2(b) at $t = 3.72$], whereas close to the sphere for $\mathrm{We} = 14$ [see inset of Fig. 2(c) at $t = 2.96$]. Note that the sphere keeps rising with $U_s > 0$ when pinch-off happens for $\mathrm{We} = 12, 14$, as shown in Fig. 2(d). These two cases therefore belong to the lower ($\mathrm{We} = 12$) and upper pinch-off penetration regime ($\mathrm{We} = 14$), respectively. In Fig. 2(e), we also present the evolution of the interface top position H, showing that it is slightly above the sphere, both H and H_s have almost identical evolutions. Since H begins with the value 0, we use for convenience H instead of H_s to investigate the dynamics henceforth.

B. Critical Weber numbers

The critical Weber numbers separating the three regimes are defined as the penetration Weber number $\mathrm{We}_{\mathrm{pen}}$ and the switching Weber number $\mathrm{We}_{\mathrm{swit}}$. For the Bond number $\mathrm{Bo} = 0.1$ in Fig. 2, the two critical numbers are $\mathrm{We}_{\mathrm{pen}} = 11.5$ and $\mathrm{We}_{\mathrm{swit}} = 12.5$. As one can expect, the two critical Weber numbers should be functions of the Bond number Bo, as obtained and presented in Fig. 3.

Note $\mathrm{We_{pen}}$ and $\mathrm{We_{swit}}$ are obtained by varying We while controlling Bo, and the accuracy of the critical Weber numbers is 0.1. The two critical Weber numbers separate the dynamics into the three regimes, and the corresponding sketches at the maximum height are shown on the right of Fig. 3. The two critical numbers decrease slightly with increasing Bo for low-gravity cases with $\mathrm{Bo} \leqslant 0.1$, while they increase dramatically with Bo for $\mathrm{Bo} > 0.1$. The decrease of $\mathrm{We_{pen}}$ for small spheres with $\mathrm{Bo} \leqslant 0.1$ is due to the decrease of the energy dissipation, which will be discussed in Sec. IV A. For large spheres with $\mathrm{Bo} \gg 1$, the penetration Weber number $\mathrm{We_{pen}}$ will finally tend to increase linearly with Bo due to the increase of gravitational potential energy, as reported experimentally by Kim *et al.* [1].

IV. DISCUSSIONS

In this section we investigate the details of the exit dynamics, including the energy evolutions, the coating dynamics, and the pinch-off dynamics. Influences of the impact velocity and gravity are discussed, and a simple model is introduced to explain the underlying mechanism of the energy conversion.

A. Energy evolutions

During the exit process, the sphere position, the sphere velocity, the bath interface, and the bath velocity fields evolve continuously, which induces the evolution of energies. To study the exit dynamics, we consider the energies of the entire system, including both the bath and the sphere. The kinetic energy E_k, the surface energy E_{ps}, the gravitational potential energy E_{pg}, and the mechanical energy E_{mech} are respectively defined as

$$E_k = \pi \int_\Omega \left(v_r^2 + v_z^2\right) r dS + \frac{2}{3}\pi U_s^2, \quad E_{\mathrm{ps}} = 2\pi \int_{\Sigma_{\mathrm{surf}}} r dl - \pi L_b^2,$$
$$E_{\mathrm{pg}} = \mathrm{Bo}\left[2\pi \int_\Omega rz dS + \frac{4}{3}\pi (H_s - 1) + \frac{1}{2}\pi L_b^4\right], \quad E_{\mathrm{mech}} = E_k + E_{\mathrm{ps}} + E_{\mathrm{pg}}, \tag{17}$$

with dS is the surface element. The two terms of E_k represent the kinetic energies respectively of the bath and the sphere, E_{ps} represents the surface energy variation between the transient value $\int_{\Sigma_{\mathrm{surf}}} 2\pi r dl$ and the initial value πL_b^2, and E_{pg} represents the gravitational potential energy variation between the transient value $\mathrm{Bo}[\int_\Omega 2\pi rz dS + \frac{4}{3}\pi (H_s - 1)]$ (where $H_s - 1$ is the coordinate of the sphere center) and the initial value $-\frac{1}{2}\pi \mathrm{Bo} L_b^4$. All energies have been nondimensionalized by $\gamma \bar{R}^2$. Note that all the energy evolutions presented in this section are for the rising phase for focusing on the exit dynamics.

We first investigate the influence of the impact velocity, described by the impact Weber number We. The energies varying with H for different We are presented in Fig. 4(a). It shows that the kinetic energy E_k decreases while the surface and potential energies increase with H, indicating that the energy conversion from E_k to E_{ps} and E_{pg}. The mechanical energy E_{mech} decreases relatively rapidly in the partial exit stage ($H \leqslant 2$) due to the strong shearing effect caused by the partially submerged sphere and decreases much slower in the full exit stage ($H > 2$). Similar evolution of the energy dissipation has also been found in droplet impact on a liquid bath [37]. Besides, in Fig. 4(a), we notice that E_{ps} and E_{pg} for different We follow similar evolutions with H, where E_{ps} and $E_{\mathrm{pg}}/\mathrm{Bo}$ depend only on the instantaneous geometry of the bath [see (17)]. This indicates that exit processes for different We follow the same trend, namely a geometrically governed evolution, independently of the impact Weber number. To unravel the mechanism, the two energies are plotted in Fig. 4(b) in a log-log plot. It shows that both E_{ps} and $E_{\mathrm{pg}}/\mathrm{Bo}$ follow approximately the square power laws of H in the partial exit stage, i.e.,

$$E_{\mathrm{ps}} \propto H^2, \quad \text{and} \quad \frac{E_{\mathrm{pg}}}{\mathrm{Bo}} \propto H^2, \quad \text{for } H \leqslant 2, \tag{18}$$

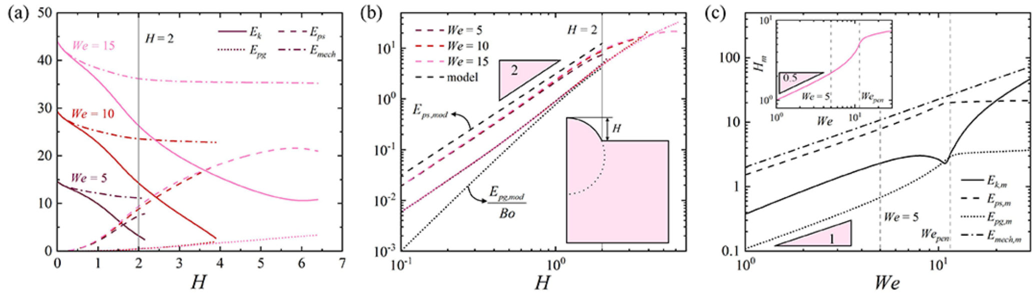

FIG. 4. Influences of the impact velocity for a typical Bond number Bo = 0.1 for the rising phase. (a) The kinetic energy E_k, the surface energy E_{ps}, the gravitational potential energy E_{pg}, and the mechanical energy E_{mech} varying with H. (b) Comparison between E_{ps} (in dashed lines) and the rescaled gravitational potential energy E_{pg}/Bo (in dotted lines), with the simple model (19), where the inset shows the simple model details. (c) The energies for the maximum height $E_{k,m}$, $E_{ps,m}$, $E_{pg,m}$, and $E_{mech,m}$ varying with the impact Weber number We, where the inset shows the maximum interface top position H_m.

which verify the above speculation. Here we give a simple model to interpret the geometry development instead of using the complicated series solution obtained in previous works [21,22], shown in the inset of Fig. 4(b). The corresponding surface energy $E_{ps,mod}$ and the rescaled gravitational potential energy $E_{pg,mod}/\mathrm{Bo}$ can be obtained respectively as

$$E_{ps,mod} = \pi H^2, \quad \text{and } E_{pg,mod}/\mathrm{Bo} = \frac{\pi}{12}H^3(4-H), \quad \text{for } 0 \leqslant H \leqslant 2, \tag{19}$$

as presented in Fig. 4(b). The derivation of $E_{ps,mod}$ and $E_{pg,mod}$ are presented in Appendix C. For the surface energy E_{ps}, our simple model predicts well the power law $E_{ps} \propto H^2$ while overestimates the value by 40%, namely $E_{ps,mod} \approx 1.4E_{ps}$. For the rescaled potential energy E_{pg}/Bo, our model predicts well the tendency for $1 < H < 2$ while it underestimates the value for $H < 1$. The deviations are because of the meniscus between the sphere bottom and the bath, as shown Figs. 2(a)–2(c).

To show the variation with respect to We, we define the energies and the interface top position when the sphere reaches the maximum height, presented in Fig. 4(c) with the subscript $()_m$. For We < 5, the processes only experience the partial exit stage [see Fig. 2(e)]. Since gravity has weak effects (Bo = 0.1), the initial kinetic energy ($\propto$ We) mainly converted into the surface energy, leading to $E_{ps,m} \propto$ We. Using the power laws (18) in the partial exit stage, the maximum height can be determined as $H_m \propto \mathrm{We}^{1/2}$ for We < 5 [see inset of Fig. 4(c)], which then further leads to $E_{pg,m} \propto$ We. For We $\approx \mathrm{We}_{pen}$, H_m increases faster with We while $E_{k,m}$ has a decrease, which are apparently due to the pinch-off. In the penetration regimes with We $> \mathrm{We}_{pen}$, $E_{mech,m}$ still increases linearly with We and is mainly composed of $E_{k,m}$, while $E_{ps,m}$ tends to a plateau.

We then investigate the influence of gravity, described by the Bond number Bo. The energies varying with H for different Bo are presented in Fig. 5(a). Note that all cases with We = 10 are in the bouncing-off regime. Different from the results in Fig. 4(a), it shows that E_{pg} increases dramatically with Bo, while the viscous dissipation decreases with Bo. Comparison between E_{ps}, E_{pg}/Bo with our simple model are shown in Fig. 5(b), showing that the power laws presented in (18) can also be observed in various gravity conditions. The energies for the maximum height are presented in Fig. 5(c), showing that $E_{k,m}$ does not vary much, and $E_{mech,m}$ is mainly composed of $E_{ps,m}$ for Bo $\leqslant 0.1$ and of $E_{pg,m}$ for Bo $\gg 0.1$, indicating that gravity begins to influence the dynamics when Bo > 0.1. Note that $E_{ps,m}$ and H_m [see inset of Fig. 5(c)] do not converge for Bo $\ll 0.1$; they actually increase slightly with Bo for Bo $\leqslant 0.1$, the corresponding mechanism is explained as follows. As shown in Fig. 5(c), $E_{mech,m}$ increases with Bo because of less energy dissipation, $E_{ps,m}$ thus increases with Bo for Bo $\leqslant 0.1$, which also corresponds to a larger H_m. This decrease of energy dissipation for

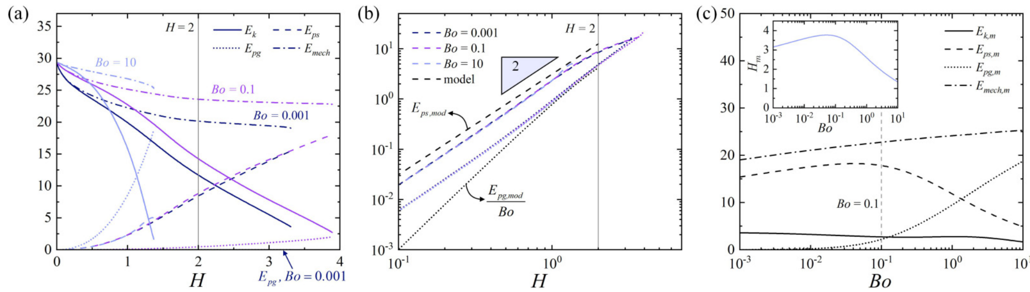

FIG. 5. Influences of gravity for a typical impact Weber number We = 10, for the rising phase. (a) The kinetic energy E_k, the surface energy E_{ps}, the gravitational potential energy E_{pg}, and the mechanical energy E_{mech}, varying with H, where E_{pg} for Bo = 0.001 is pointed out by the arrow. (b) Comparison between E_{ps} (in dashed lines) and the rescaled gravitational potential energy $E_{\mathrm{pg}}/\mathrm{Bo}$ (in dotted lines), with the simple model. (c) The energies for the maximum height $E_{k,m}$, $E_{\mathrm{ps},m}$, $E_{\mathrm{pg},m}$, $E_{\mathrm{mech},m}$ varying with Bo, where the inset shows the comparison between H_m, $E_{\mathrm{ps},m}^{1/2}$, and $(E_{\mathrm{pg},m}/\mathrm{Bo})^{1/2}$.

Bo $\leqslant 0.1$ further means that less initial kinetic energy is needed to achieve the penetration, namely $\mathrm{We}_{\mathrm{pen}}$ decreases with Bo, as presented in Fig. 3.

B. Coating dynamics

During the rising phase of the sphere, the interface $(r_{\mathrm{surf}}, z_{\mathrm{surf}})$ deforms along the sphere and forms a coated layer $h(\theta, t)$, as presented in Fig. 1(b), where h and θ are respectively defined as

$$h = \sqrt{[z_{\mathrm{surf}} - (H_s - 1)]^2 + r_{\mathrm{surf}}^2} - 1, \quad \text{and} \ \ \theta = \arcsin \frac{r_{\mathrm{surf}}}{h+1}. \tag{20}$$

A typical time evolution is plotted in Figs. 6(a)–6(c) for We = 10 and Bo = 0.1; Fig. 6(a) shows the pressure field, while Figs. 6(b) and 6(c) show respectively the layer thickness $h(\theta, t)$ and the pressure distribution $p(\theta, t)$ on the sphere for different time steps. All the variables presented in this section are for the rising phase. For convenience, we define the layer thickness at $\theta = 0^\circ$ as h_{0° ($h_{0^\circ} = H - H_s$) and the minimum thickness as $h_{\min}$ with the corresponding angle $\theta_{\min}$, as presented in Fig. 6(a). Note that we define the coated layer to be in the range of $0^\circ \leqslant \theta \leqslant \theta_{\min}$. Here we use the full interface profile in (20) to obtain the continuous thickness function $h(\theta, t)$. The volume of the coated layer V_{coat} is defined as

$$V_{\mathrm{coat}} = \int_0^{\theta_{\min}} 2\pi h \sin\theta d\theta, \tag{21}$$

and the maximum value is defined as $V_{\mathrm{coat,max}}$. As presented in Fig. 6(a), the coated layer is entrained in the partial exit stage and turns to be relatively thick above the apex and thin around the equator after it enters the full exit stage. Figure 6(b) shows that h_{0° stays around 0.1 while $h_{\min}$ (represented by the circles) gradually decreases to 0.01 with the final $\theta_{\min} \approx 100^\circ$. The pressure field in Fig. 6(a) shows that the pressure is relatively high in the coated layer, whose value keeps $p \approx 2$ [see Fig. 6(c)], and suddenly decreases at the position around $\theta_{\min}$. This indicates the fact that both axial and radial curvatures approximate 1 in the coated layer (in the dimensional form, $1/\bar{R}$), and the axial curvature decreases to negative for $\theta > \theta_{\min}$.

Influences of the impact velocity on the coated layer are presented in Fig. 7. We here mainly consider the evolution of the coated volume, whose maximum status $V_{\mathrm{coat,max}}$ is pointed out by circle in Figs. 7(a)–7(d). As shown in Fig. 7(a), the coated volume V_{coat} only increases in the partial exit stage with $H \leqslant 2$ and decreases due to the capillary drainage after entering the full exit stage. During the increase of V_{coat}, the angle $\theta_{\min}$ keeps increasing, h_{0° remains at the order of 0.1 for large We while it decreases with H for small We, and $h_{\min}$ decreases monotonically with We. It should be

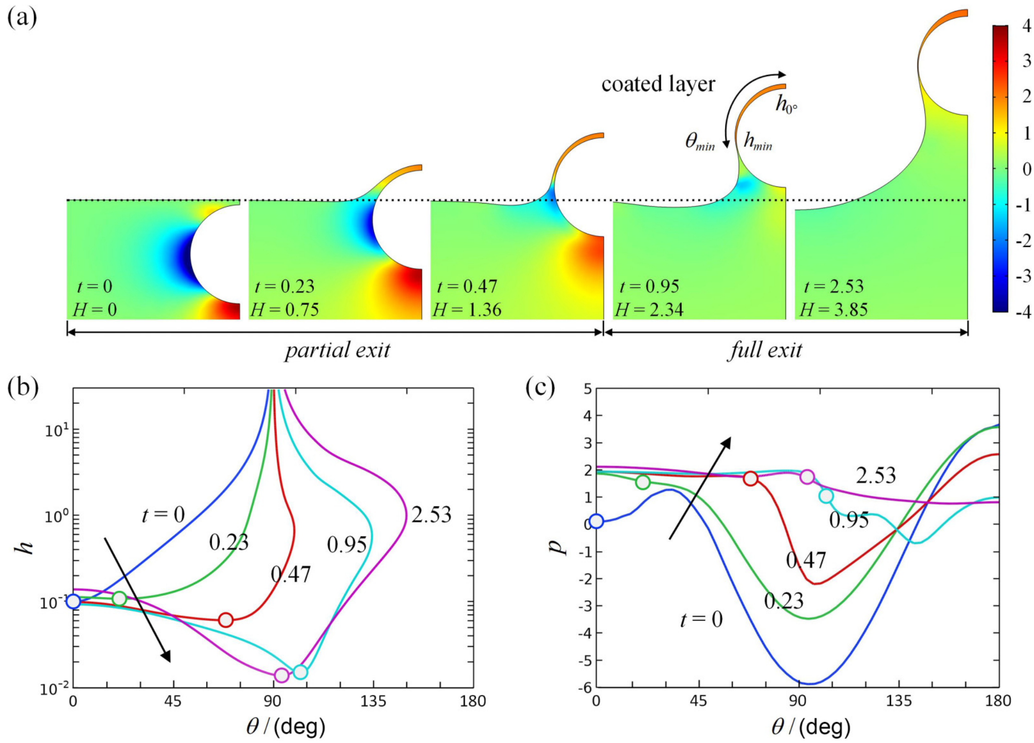

FIG. 6. Evolutions of the coated layer for the rising phase for a typical case with We = 10 and Bo = 0.1. (a) Typical time steps, the color indicates the pressure field, the dotted line represents the position of the initial flat surface. [(b) and (c)] The coated layer thickness $h(\theta, t)$ and the pressure distribution $p(\theta, t)$ on the sphere at different time steps; the circle represents $h_{\min}$ and $\theta_{\min}$, and the arrow indicates the time evolution.

noted that $\theta_{\min}$ becomes around 90° for large We, namely only the upper half of the sphere is coated tightly by the liquid. To show the influences of the impact velocity more quantitatively, we plot $V_{\text{coat,max}}$ varying with We in Fig. 7(f) and the corresponding sketches in Fig. 7(e). For increasing impact velocity, $V_{\text{coat,max}}$ first increases linearly with We, i.e., $V_{\text{coat,max}} \propto \text{We}$ for small We, and tends to a constant for large We. The mechanism is interpreted as follows. Let us define H_{Vmax}, $\theta_{\text{min,Vmax}}$, $h_{0^\circ,\text{Vmax}}$, and $h_{\text{min,Vmax}}$ as the height, the angle of the minimum layer thickness, the layer thickness at the apex, and the minimum layer thickness corresponding to $V_{\text{coat,max}}$, respectively. For small impact velocities, the maximum volume $V_{\text{coat,max}}$ occurs at $H_{\text{Vmax}} \sim H_m$ [see Fig. 7(a)], which leads to $H_{\text{Vmax}} \propto \text{We}^{1/2}$ [note $H_m \propto \text{We}^{1/2}$ is presented in the inset of Fig. 4(c)]. This can also be found in Fig. 7(b) as $\theta_{\text{min,Vmax}}$ increases with We. On the other hand, $h_{0^\circ,\text{Vmax}}$ and $h_{\text{min,Vmax}}$ increase with We [see inset of Fig. 7(f)], and $h_{0^\circ,\text{Vmax}} \propto \text{We}^{1/2}$ can be found for small We. Since the thickness of coated layer should be mainly determined by $h_{0^\circ,\text{Vmax}}$ at the apex, the maximum volume thus can be estimated as $V_{\text{coat,max}} \sim \pi H_{\text{Vmax}} h_{0^\circ,\text{Vmax}}$, leading to $V_{\text{coat,max}} \propto \text{We}$. Note that πH_{Vmax} is the dimensionless coated area. For large impact velocities, the maximum volume occurs at $H_{\text{Vmax}} \approx 2$ [see Fig. 7(a)], and the coated layer thickness is limited to $h_{0^\circ,\text{Vmax}} \sim 0.1$ since the launch position is $H_{s,0} = -0.1$ [see inset of Fig. 7(f)]. The maximum volume thus can be estimated as $V_{\text{coat,max}} \sim 0.2\pi$, as shown in the dashed line in the inset of Fig. 7(f).

Influences of gravity on the coated layer are presented in Fig. 8, where the maximum status $V_{\text{coat,max}}$ is also pointed out by circle in Figs. 7(a)–7(d). It shows that, with the larger gravity effect, $V_{\text{coat,max}}$ occurs at a lower height H_{Vmax} and its value is smaller and $\theta_{\text{min,Vmax}}$ remains around 90°. For the layer thickness, the gravity effect can be observed when Bo = 10, for which h_{0° decreases

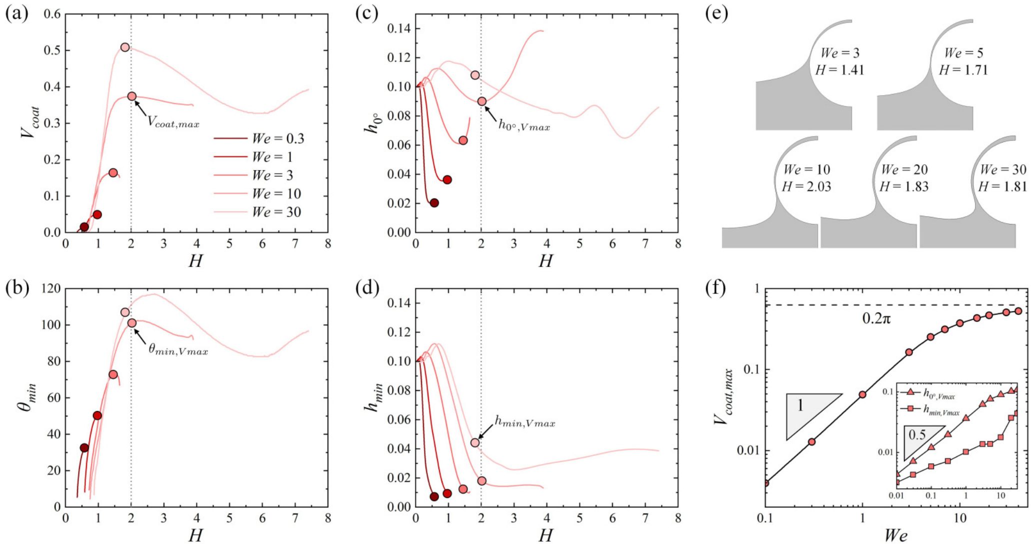

FIG. 7. Influences of the impact velocity for a typical Bond number Bo $= 0.1$ for the rising phase. [(a)–(d)] Transient values varying with H for different We: the volume of the coated layer V_{coat} in (a), the angle for minimum thickness $\theta_{\min}$ in (b), the layer thickness above the apex h_{0° in (c), and the minimum layer thickness $h_{\min}$ in (d), where the circle indicates the status for the maximum volume $V_{\text{coat,max}}$. (e) The sketches of the coated layer at the maximum volume $V_{\text{coat,max}}$. (f) The maximum volume $V_{\text{coat,max}}$ varying with We; the inset shows $h_{0^\circ,\text{Vmax}}$ and $h_{\min,\text{Vmax}}$ varying with We.

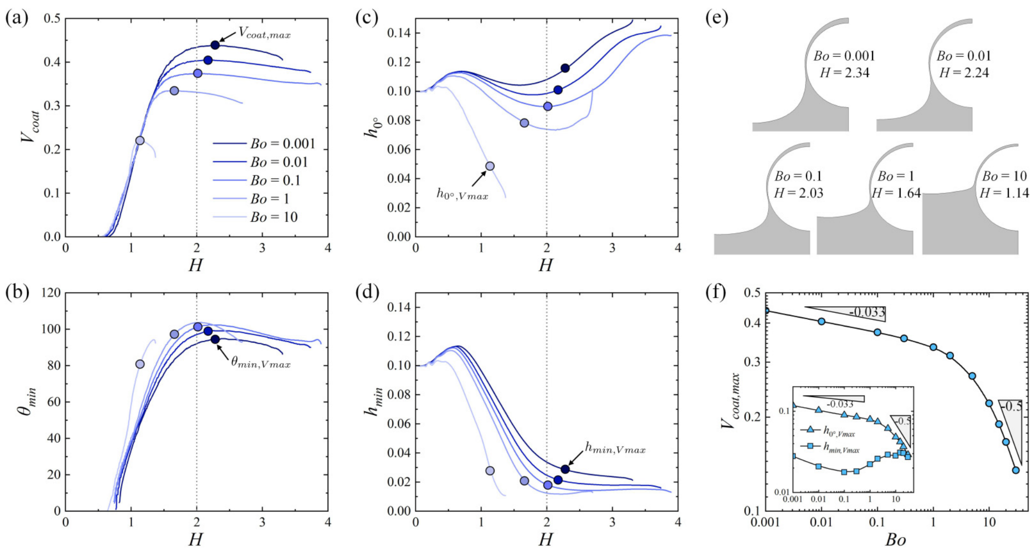

FIG. 8. Influences of gravity for a typical impact Weber number We $= 10$ for the rising phase. [(a)–(d)] Transient values varying with H for different We: the volume of the coated layer V_{coat} in (a), the angle for minimum thickness $\theta_{\min}$ in (b), the layer thickness above the apex h_{0° in (c), and the minimum layer thickness $h_{\min}$ in (d), where the circle indicates the status for the maximum volume $V_{\text{coat,max}}$. (e) The sketches of the coated layer at the maximum volume $V_{\text{coat,max}}$. (f) The maximum volume $V_{\text{coat,max}}$ varying with Bo; the inset shows $h_{0^\circ,\text{Vmax}}$ and $h_{\min,\text{Vmax}}$ varying with Bo.

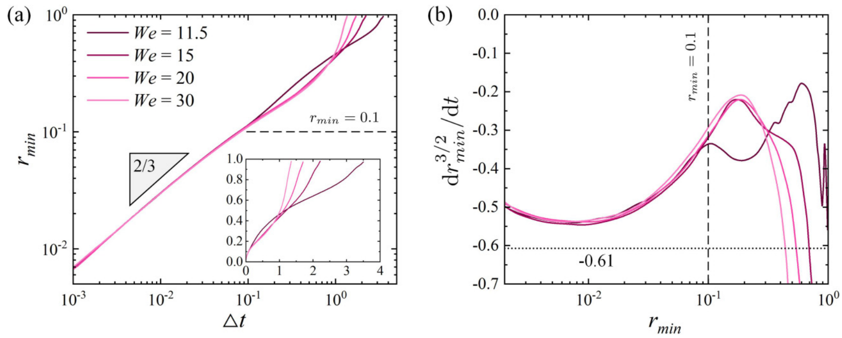

FIG. 9. Pinch-off behavior of different impact We with Bo $= 0.1$. (a) The minimum ligament radius $r_{\min}$ in log scale varying with the time distance Δt to pinch-off in log scale, the inset shows both axes in linear scale. (b) The derivative of $r_{\min}^{3/2}$ with respect to time t, versus $r_{\min}$; the dotted line represents $dr_{\min}^{3/2}/dt = -0.61$. The dashed lines in (a) and (b) represent $r_{\min} = 0.1$.

dramatically with H [see Fig. 7(c)]. The sketches and the maximum volume $V_{\text{coat,max}}$ are presented in Figs. 8(e) and 8(f), respectively. It shows that $V_{\text{coat,max}}$ keeps decreasing with larger Bo, and two power laws can be observed, namely $V_{\text{coat,max}} \propto \text{Bo}^{-0.033}$ for Bo $\leqslant 0.1$ and $V_{\text{coat,max}} \propto \text{Bo}^{-0.5}$ for Bo $\gg 0.1$. Since the coated area (determined by $\theta_{\text{min,Vmax}} \sim 90^\circ$) is generally 2π, the coated volume thus depends only on the layer thickness. As presented in the inset of Fig. 8(f), the two power laws hold also for the layer thickness. For Bo $\leqslant 0.1$, both $h_{0^\circ,\text{Vmax}}$ and $h_{\text{min,Vmax}}$ decrease slightly with Bo, whose tendencies generally fit $\propto \text{Bo}^{-0.033}$. For Bo $\gg 0.1$, $h_{0^\circ,\text{Vmax}}$ decreases rapidly with Bo with $h_{0^\circ,\text{Vmax}} \propto \text{Bo}^{-0.5}$. It should be noted that with larger Bo, the difference between $h_{0^\circ,\text{Vmax}}$ and $h_{\text{min,Vmax}}$ decreases, which indicates that the gravity effect uniforms the coated layer, as illustrated in Fig. 8(e).

C. Pinch-off dynamics

In the penetration regimes, when the minimum radius of the ligament turns much smaller than the sphere size, namely $r_{\min} \ll 1$, pinch-off happens. We first consider the local pinch-off behavior. Since the Ohnesorge number we considered in the present paper satisfies Oh $\leqslant 0.013$, the ligament first enters the inertia pinch-off regime [38–40] with the self-similar behavior $r_{\min} = 0.717\Delta t^{2/3}$, where $\Delta t = t_p - t$ is the time distance to the final pinch-off, the coefficient 0.717 holds in the inviscid limit [41]. We plot pinch-off behaviors for typical cases in Fig. 9 for $r_{\min} \geqslant 0.002$. Note the case where We $= 11.5$ belongs to the lower pinch-off penetration regime and the cases where We $= 15$, 20, 30 belong to the upper pinch-off penetration regime. As presented in Fig. 9(a), $r_{\min}$ decreases as Δt decreases for different We, and they converge to the same curve with the 2/3 power law when $r_{\min} < 0.1$. The inset of Fig. 9(a) shows that the time distance Δt corresponding to $r_{\min} = 1$ is smaller for larger We, which is in line with the fact that a faster stretching induces a stronger radial contraction. To show the entering of the pinch-off phase more clearly, we transform the power law into $r_{\min}^{3/2} = 0.61(t_p - t)$ [40]. As presented in Fig. 9(b), $dr_{\min}^{3/2}/dt$ begins to decrease when $r_{\min} < 0.1$ and reaches the minimum value $dr_{\min}^{3/2}/dt \approx -0.54$ at $r_{\min} \approx 0.01$. The deviation between -0.54 and -0.61 is because of the viscous effect, as reported in Ref. [41]. One should also note that the ligament later exits the inertia pinch-off regime [see $r_{\min} < 0.01$ in Fig. 9(b)], then enters the viscous regime, and finally ends up with the inertia-viscous pinch-off regime [38]. Considering both the precision and the computing time, we stop the simulation at $r_{\min} = 0.01$, and the corresponding time is regarded as the pinch-off time t_p in the present paper.

The axial stretching determines whether the pinch-off occurs or not, as presented in Fig. 2. To show the role of the axial sphere motion on the radial contraction of the ligament, the evolution

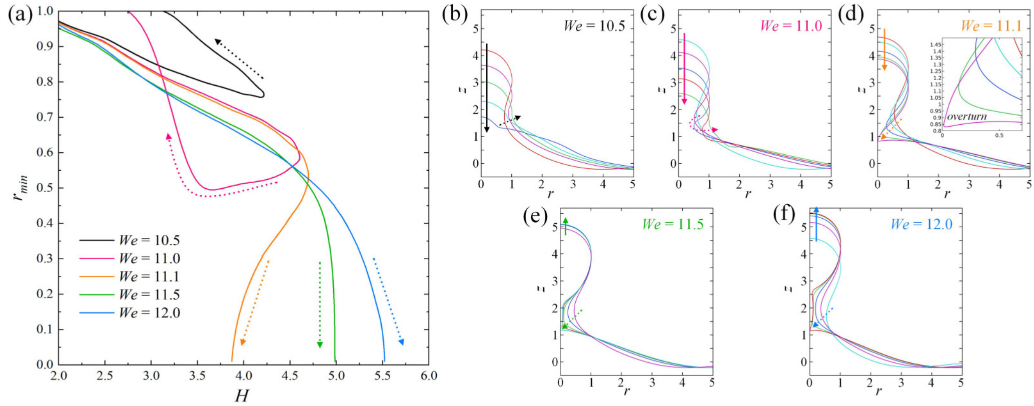

FIG. 10. (a) The minimum radius $r_{\min}$ varying with H for different We around $\mathrm{We}_{\mathrm{pen}} = 11.5$ for $\mathrm{Bo} = 0.1$. [(b)–(f)] The interface evolutions of the cases shown in (a); the descending phase for $\mathrm{We} = 10.5, 11.0, 11.1$; and the rising phase for $\mathrm{We} = 11.5, 12.0$. The solid arrows indicate the descending or rising phases, respectively, while the dotted arrows indicate the corresponding trajectories of $r_{\min}$.

of the minimum radius $r_{\min}$ with H are presented in Fig. 10 for $\mathrm{Bo} = 0.1$ and different values of We around $\mathrm{We}_{\mathrm{pen}} = 11.5$. Differences occur when the sphere is close to its maximum height. The evolutions of $r_{\min}$ are pointed out with dotted arrows in Fig. 10(a), and the evolutions of the profile are presented in Figs. 10(b)–10(f). As presented in Fig. 10(b) with $\mathrm{We} = 10.5$, after the transition into the descending, the interface falls down and flattens, while its minimum radius increases [see also Fig. 10(a)]. For $\mathrm{We} = 11.0$, as shown in Fig. 10(c), the ligament first contracts and then expands during the descending phase, and the corresponding $r_{\min}$ thus first decreases then increases [also see Fig. 10(a)]. Pinch-off occurs when the impact velocity increases, as shown in Figs. 10(d)–10(f) for $\mathrm{We} = 11.1$, 11.5, and 12.0. The ligament is stretched long enough to trigger the capillary instability and finally ends with pinch-off. The difference is that pinch-off happens during the descending phase for $\mathrm{We} = 11.1$, happens just at the time the sphere stops for $\mathrm{We} = 11.5$, and happens during the rising phase for $\mathrm{We} = 12.0$, as pointed out by the dotted arrows in Fig. 10(a). It is worth noting that Fig. 10(d) shows that pinch-off could occur during the descending phase for $\mathrm{We} \lesssim \mathrm{We}_{\mathrm{pen}}$, namely after the sphere is bounced downwards by the interface, which is thus classified as the bouncing-off regime. In the inset of Fig. 10(d), we also show the overturn phenomenon, which is a geometrical feature of the inertia pinch-off regime.

When the impact velocity is even higher, as introduced in Sec. III B, the pinch-off switching occurs. The difference between the two critical Weber numbers, $\mathrm{We}_{\mathrm{swit}} - \mathrm{We}_{\mathrm{pen}}$, varying with Bo is presented in Fig. 11(a). Note the accuracy of $\mathrm{We}_{\mathrm{swit}} - \mathrm{We}_{\mathrm{pen}}$ is 0.2. The difference keeps coincidently $\mathrm{We}_{\mathrm{swit}} - \mathrm{We}_{\mathrm{pen}} \approx 1$ for $\mathrm{Bo} \leqslant 0.1$, then increases with Bo for $\mathrm{Bo} > 0.1$, and finally tends to $\mathrm{We}_{\mathrm{swit}} - \mathrm{We}_{\mathrm{pen}} \propto \mathrm{Bo}$ for $\mathrm{Bo} \gg 0.1$ [see inset of Fig. 11(a)]. To show the details of the switching, we plot evolutions of the interface profile and the axial velocity at $r = 0$ for $\mathrm{We} = 11.5$, 12.5, 13.5 in Fig. 12. The pinch-off location is defined as z_p, pointed out by arrows in Figs. 12(a)–12(c). In Fig. 11(b), we show that when $\mathrm{Bo} = 0.1$, the pinch-off location z_p stays at $z_p \approx 1$ for $11.5 \leqslant \mathrm{We} \leqslant 12.4$ and switches to $z_p \approx 3$ at $\mathrm{We} = 12.5$ and then increases with We. The switching mechanism is stated as follows. As shown in the literature [31,42,43], the ligament can be well described by the one-dimensional model before overturning [see Fig. 10(d)]. We here introduce the dimensionless continuity equation, written in the following form:

$$D_t(\ln r_{\mathrm{surf}}) + \tfrac{1}{2}\partial_z v_z = 0, \tag{22}$$

where D_t represents the material derivative and v_z is assumed to be r independent in the ligament. This equation indicates that location with large $\partial_z v_z$ leads to a strong contraction [large $D_t(\ln r_{\mathrm{surf}})$],

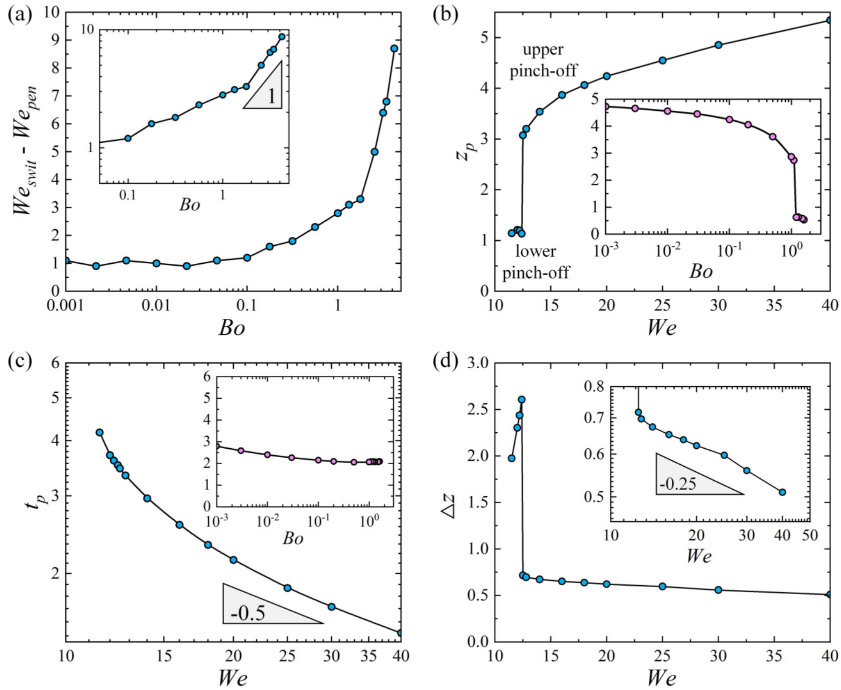

FIG. 11. (a) $We_{swit} - We_{pen}$ in linear scale varying with the Bond number Bo in log scale; the inset shows both axes in log scales. (b) The pinch-off location z_p varying with the impact Weber number We for Bo = 0.1; the inset shows z_p varying with the Bond number Bo for We = 20. (c) The pinch-off time t_p varying with the impact Weber number We for Bo = 0.1, the inset shows t_p varying with the Bond number Bo for We = 20. (d) The distance Δz from the pinch-off position to the sphere bottom at the pinch-off instant, varying with the impact Weber number We, the inset shows both axes in log scales.

defined as the upper suction or lower drainage locations, as shown by arrows in Fig. 12. As shown in Figs. 12(a) and 12(d), for We = 11.5, the lower drainage is stronger than the upper suction, leading to a lower pinch-off. Since Bo = 0.1 in Fig. 12, the gravity effect is negligible (as discussed in Sec. IV A), and the lower drainage thus is induced by the capillary forces. As the impact velocity increases, the upper suction turns stronger, which just overcomes the lower drainage at We = 12.5 and leads to the almost-simultaneous pinch-off, as shown in Figs. 12(b) and 12(e). For an even larger impact velocity, e.g., We = 13.5 in Figs. 12(c) and 12(f), the upper suction is much stronger than the lower drainage, and the upper pinch-off thus happens first. It should also be mentioned that the ligament falls back to the bath after pinch-off, which could further induce a cavity and a jet [44]. The inset of Fig. 11(b) shows the gravity effect on z_p for We = 20, showing that z_p decreases with Bo, and switches from upper to lower at Bo ≈ 1. Now, let us consider again Fig. 11(a); the switching is found due to the competition between the upper suction and the lower drainage: For Bo $\leqslant$ 0.1, the lower drainage is mainly induced by the capillary forces, and $We_{swit} - We_{pen}$ is thus independent of Bo; for Bo $\gg$ 0.1, the lower drainage is mainly induced by gravity, and $We_{swit} - We_{pen}$ is thus linear with Bo.

Finally, we consider the pinch-off time t_p. As shown in Fig. 11(c), t_p decreases with We and tends to a power law $t_p \propto We^{-1/2}$ for We $\gg$ 1, indicating that the radial contraction is mainly induced by the axial stretching ($U_s \sim \sqrt{We}$). As for the gravity effect, the inset of Fig. 11(b) shows that for We = 20, t_p decreases slightly with Bo due to larger gravity drainage. Using the pinch-off time, we can predict the pinch-off position by the concept of decay length [29,45]. Duchemin *et al.* [45] studied a ligament with an impulsive axial motion on one side and showed that the axial depth at

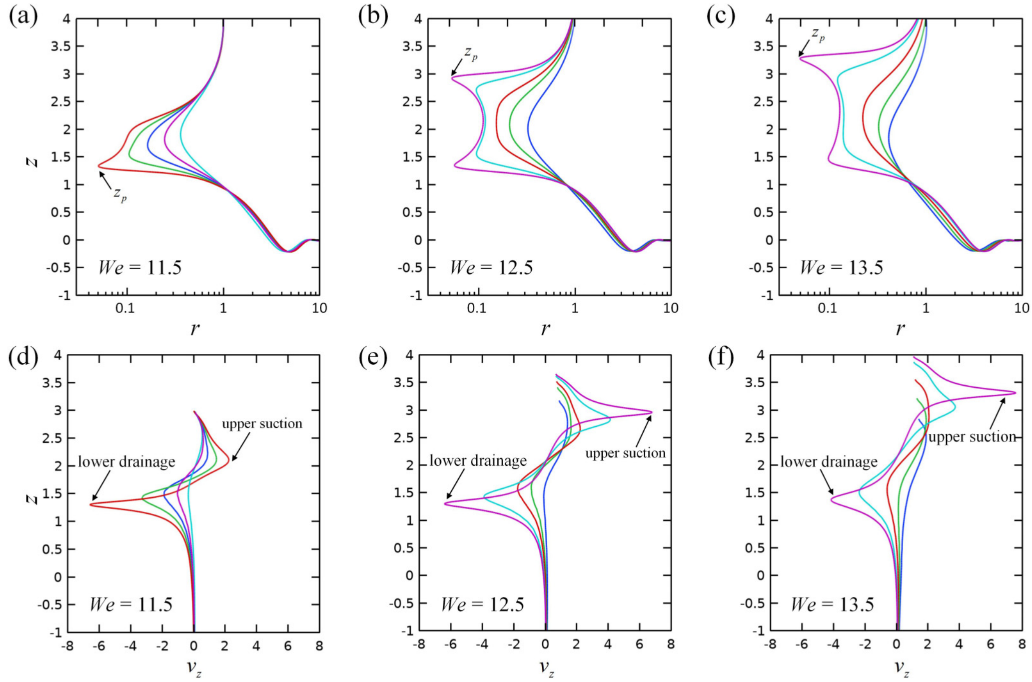

FIG. 12. Evolutions for the interface profile and the axial velocity at $r = 0$ for We $= 11.5$ in [(a) and (d)], 12.5 in [(b) and (e)], and 13.5 in [(c) and (f)] with Bo $= 0.1$. The pinch-off location z_p is pointed out in (a)–(c), and the lower drainage and the upper suction locations are pointed out in (d)–(f).

which the liquid is affected by the motion (denoted λ) is proportional to $\sqrt{t}$, i.e., $\lambda \propto \sqrt{t}$. Kim *et al.* [29] studied the pinch-off behavior of a ligament attached to an accelerating sphere from a bath. They discussed this axial depth and found that it agrees satisfactorily with $\lambda \propto \sqrt{t}$. We here show the distance Δz from the pinch-off position to the sphere bottom varying with We in Fig. 11(d), where $\Delta z = H_m - z_p - 2$. The distance increases with We for lower pinch-off cases, while it decreases slightly with We for upper pinch-off cases, the latter shows a power law $\Delta z \propto \mathrm{We}^{-1/4}$ [see inset of Fig. 11(d)]. The mechanism of the $-1/4$ power law are stated as follows. For the attached ligament, the stretching motion stabilizes the ligament [31], which indicates that capillary instability is triggered at a position where the stretching motion decays to zero. The distance thus can be estimated as $\Delta z \sim \lambda_p$, where $\lambda_p \propto \sqrt{t_p}$ is the axial position of the pinch-off. For large impact Weber numbers, applying the power law $t_p \propto \mathrm{We}^{-1/2}$, one obtains $\Delta z \propto \mathrm{We}^{-1/4}$.

V. CONCLUSIONS

In this paper the exit dynamics of a sphere launched underneath a liquid bath surface has been described by means of a nonstationary two-dimensional model. The exit process is sequenced into a partial exit stage for the interface top position $H \leqslant 2$ and a full exit stage for $H > 2$. In the partial exit stage, the interface on the sphere is elevated and deforms into a coated layer. In the full exit stage, a ligament is formed and stretched by the rising sphere. The dynamics can be separated into a bouncing-off regime, a lower pinch-off penetration regime, and an upper pinch-off penetration regime, depending on the impact Weber number We and the Bond number Bo. The differences between the dynamic regimes are the occurrence and the location of pinch-off. With an increasing Bo, the penetration Weber number $\mathrm{We}_{\mathrm{pen}}$ and the switching Weber number $\mathrm{We}_{\mathrm{swit}}$ first decrease slightly with Bo for Bo $\leqslant 0.1$ and then increase with Bo for Bo > 0.1.

The energy evolutions, the coating dynamics, and the pinch-off dynamics are studied separately. The energy evolutions shows that the impact kinetic energy E_k mainly converts into the surface energy E_{ps} for low-gravity cases with $\mathrm{Bo} \leqslant 0.1$ and into the gravitational potential energy E_{pg} for large-gravity cases with $\mathrm{Bo} \gg 0.1$. A simple model is demonstrated to show that the energies satisfy $E_{\mathrm{ps}} \propto E_{\mathrm{pg}}/\mathrm{Bo} \propto H^2$ in the partial exit stage. The coated layer is defined as the liquid that coats tightly on the sphere, which is entrained during the partial exit stage and essentially occurs on the upper hemisphere. The maximum coated volume increases linearly with the impact Weber number for slow impact and tends to constant for fast impact, the latter is related to the launch depth. The breakup of the ligament happens due to the triggering of capillary instability, which ends up with pinch-off. The switching between the lower and upper pinch-off locations is shown as the result of the competition between the upper suction and the lower drainage, the latter being dominated by capillary forces for low-gravity cases with $\mathrm{Bo} \leqslant 0.1$ or by gravity for large-gravity cases with $\mathrm{Bo} \gg 0.1$. The difference between $\mathrm{We}_{\mathrm{swit}}$ and $\mathrm{We}_{\mathrm{pen}}$, namely $\mathrm{We}_{\mathrm{swit}} - \mathrm{We}_{\mathrm{pen}}$, is independent of Bo for $\mathrm{Bo} \leqslant 0.1$, and increases with Bo for $\mathrm{Bo} > 0.1$. Finally, the pinch-off time t_p was found to decrease with both We and Bo, and a power law $t_p \propto \mathrm{We}^{-1/2}$ is observed for $\mathrm{We} \gg 1$ due to the dominant of stretching contraction.

ACKNOWLEDGMENTS

This work was supported by the National Natural Science Foundation of China [(X.W.) Grant No. 12202399, (D.W.) Grant No. 52375068, and (D.L. Grant No. 12302355)], Natural Science Foundation of Zhejiang Province [(X.W.) Grant No. LY24A020004 and (F.L.) Grant No. LD22E050003)], and B.S. thanks the F.R.S.-FNRS for financial support.

APPENDIX A: VALIDATION OF THE MODEL

In this Appendix, we validate our model for both the resistive force and the interface profile. To validate the resistive force exerted on the sphere during the exit dynamics, we compute first the resistive force of a sphere in a very large bath with negligible gravity, i.e., as in an infinite medium. In practice we set the Bond number $\mathrm{Bo} = 10^{-3}$, the bath size $L_b = 10^4$, and the initial sphere position $H_{s,0} = -5 \times 10^3$, and the sphere velocity U_s is set to be a constant. The resistive force F is obtained using (6), which converges to a constant value at sufficiently large time, from which we can compute the drag coefficient as follows:

$$C_d = \frac{\bar{F}}{\frac{1}{2}\rho \bar{U}_s^2 \bar{S}}, \tag{A1}$$

where $\bar{S} = \pi \bar{R}^2$ is the windward area. As shown in Fig. 13(a), our numerical predictions agree well with the published data [46], which is also obtained using the axisymmetric model.

For the interface profile prediction, the two-dimensional model applied in this paper has been used to study the dynamics of a ligament drawn out of a bath [31], which agrees well with the experiments for both the interface profile and the breakup height. In addition, we compare results of our model with a published experiment of a sphere launched underneath a liquid bath surface. Kim *et al.* [1] used a spring to shoot a sphere of various diameters and densities towards the water-air interface at different velocities and angles. The comparison of profiles at the pinch-off moment is shown in Fig. 13(b) for $\rho_s/\rho = 1.34$, $\mathrm{Bo} = 0.19$, and $H_m = 6.44$, showing that our prediction agrees well with the experimental data (obtained from Fig. 1(c) in Kim *et al.* [1]).

APPENDIX B: INFLUENCE OF THE SUBMERGED STAGE

In this Appendix, we show the influence of the submerged stage. For convenience, we define the dimensionless velocity at the maximum sphere height as $U_{s,m}$ and the dimensionless maximum sphere height as $H_{s,m}$. We first investigate a sphere launched with a constant initial velocity

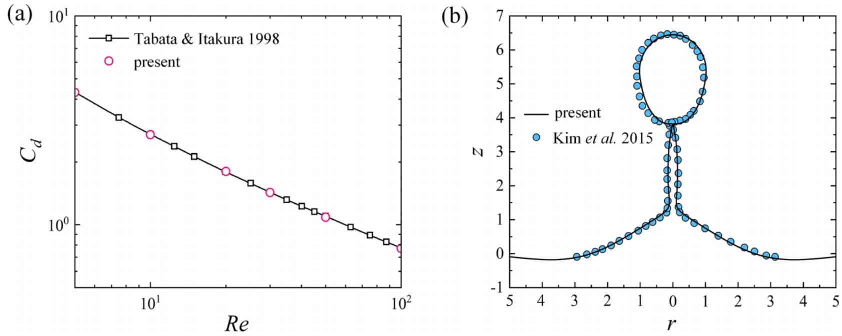

FIG. 13. Validations of the model. (a) The comparison of drag coefficient C_d between our model and the published data [46]. (b) The interface profile obtained using our model in the solid line compared with the experimental data for $\rho_s/\rho = 1.34$, $\mathrm{Bo} = 0.19$, and $H_m = 6.44$ at the pinch-off moment [1].

$U_{s,0} = 3.87$ ($\mathrm{We} = 15$) at different initial positions $H_{s,0}$. Evolutions of the transient sphere velocity U_s and the layer thickness h_{0° for the rising phase are presented in Fig. 14(a), where $h_{0^\circ} = H - H_s$. As the launch position $H_{s,0}$ becomes deeper, $U_{s,\mathrm{im}}$ decreases due to a longer submerged path, which further leads to a lower maximum height $H_{s,m}$. Cases with $H_{s,0} = -3$ and -2 are in the bouncing-off regime with $U_{s,m} = 0$, while cases with $H_{s,0} = -1$ and -0.1 are in the penetration regimes with $U_{s,m} > 0$. As presented in the inset of Fig. 14(a), the layer thickness h_{0° always tends to $h_{0^\circ} \approx 0.1$ after entering the full exit stage ($H > 2$), while it oscillates stronger for a deeper launch position. Note that the oscillation is caused by the wave induced by the submerged sphere, which corresponds to more energy loss and could induce complex rupture of the interface [4,13–15].

We then investigate the exit dynamics by controlling the impact velocity $U_{s,\mathrm{im}} = 2.83$. As presented in Fig. 14(b), the maximum sphere height $H_{s,m}$ generally increases with deeper launch positions $H_{s,0}$, and it converges for deep launch with $H_{s,0} \leqslant -5$. On the other hand, the inset of Fig. 14(b) shows that the launch velocity increases with deeper $H_{s,0}$. The increase of $H_{s,m}$ is due to the fact that the liquid around the sphere has been accelerated during the submerged rising stage, which thus exerts less resistive force on the sphere during the exit. Similar results have been reported experimentally in Refs. [13,14]. In Fig. 14(b), a new convergence region can be observed for the underneath launch with $H_{s,0} \geqslant -3$. The details of the underneath launch with the impact velocity $U_{s,\mathrm{im}} = 2.83$ are plotted in Fig. 14(c). It shows that the transient sphere velocity U_s for different $H_{s,0}$

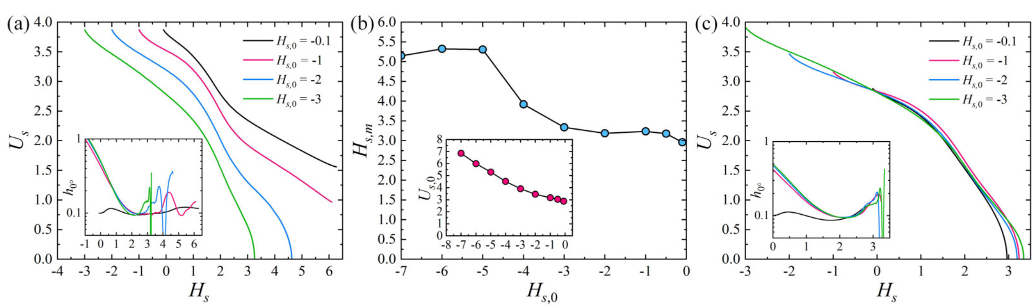

FIG. 14. [(a) and (c)] Transient sphere velocity U_s varying with the transient sphere position H_s of the rising phase, for different launch positions $H_{s,0}$, with a constant launch velocity $U_{s,0} = 3.87$ in (a) and a constant impact velocity $U_{s,\mathrm{im}} = 2.83$ in (c), where the insets show the thickness h_{0° of the coated layer above the sphere. (b) The maximum sphere height $H_{s,m}$ varying with the launch position $H_{s,0}$, with the same impact velocity $U_{s,\mathrm{im}} = 2.83$, where the inset shows the corresponding launch velocity $U_{s,0}$. All cases are for $\mathrm{Bo} = 0.1$.

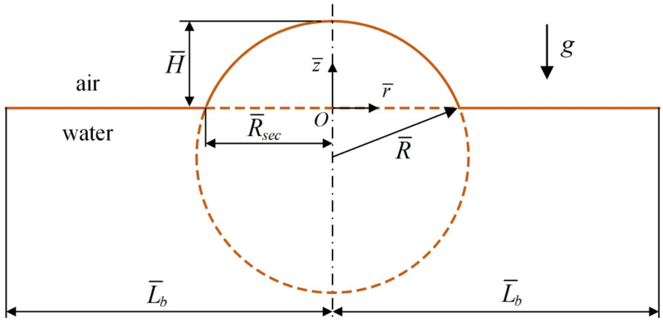

FIG. 15. Sketch of the simple model, where $\bar{L}_b$ is the bath radius and $\bar{R}$, $\bar{H}$, and $\bar{R}_{\mathrm{sec}}$ are respectively the radius, the height, and the section radius of the spherical cap.

develops in the same tendency and stops at $H_{s,m} \approx 3$. For the layer thickness h_{0°, as shown in the inset of Fig. 14(c), the evolutions are similar after entering the full exit stage ($H > 2$), and large oscillations can also be observed for $H_{s,0} = -2, -3$. These results show that for the underneath launch, the exit dynamics is reasonably independent of the launch depth if $H_{s,0} \geqslant -3$. Since the launch velocity $U_{s,0} = 2.88$ approximates the impact velocity $U_{s,\mathrm{im}} = 2.83$ for $H_{s,0} = -0.1$, we set $H_{s,0} = -0.1$ in the present paper to directly control the impact velocity.

APPENDIX C: DERIVATION OF ENERGIES FOR THE SIMPLE MODEL

In this Appendix, we show the details of the derivation for $E_{\mathrm{ps,mod}}$ and $E_{\mathrm{pg,mod}}$ based on the simple model mentioned in Sec. IV A. As shown in Fig. 15, the interface is simplified into a spherical cap and a flat surface. The radius and the height of the spherical cap are respectively $\bar{R}$ and $\bar{H}$, and the radius of the section $\bar{R}_{\mathrm{sec}}$ then can be obtained as $\bar{R}_{\mathrm{sec}} = \sqrt{\bar{R}^2 - (\bar{R} - \bar{H})^2}$. The transient interface area is $\pi(\bar{L}_b^2 - \bar{R}_{\mathrm{sec}}^2) + 2\pi\bar{R}\bar{H}$, with the initial interface area being $\pi\bar{L}_b^2$. The surface energy variation relative to the initial value thus can be obtained as

$$\bar{E}_{\mathrm{ps,mod}} = \gamma\left(2\pi\bar{R}\bar{H} - \pi\bar{R}_{\mathrm{sec}}^2\right) = \gamma\pi\bar{H}^2, \quad \text{for } 0 \leqslant \bar{H} \leqslant 2\bar{R}. \tag{C1}$$

The gravitational potential energy variation relative to the initial value is induced by the dense volume inside the spherical cap, which can be calculated as $\bar{E}_{\mathrm{pg,mod}} = \pi\rho\int_0^{\bar{H}}(\bar{r}^2\bar{z})d\bar{z}$, where $\bar{r} = \sqrt{\bar{R}^2 - (\bar{z} + \bar{R} - \bar{H})^2}$, leading to the form,

$$\bar{E}_{\mathrm{pg,mod}} = \frac{\pi\rho g}{12}\bar{H}^3(4\bar{R} - \bar{H}), \quad \text{for } 0 \leqslant \bar{H} \leqslant 2\bar{R}. \tag{C2}$$

Nondimensionalized by $\gamma\bar{R}^2$, one can finally obtain the dimensionless surface energy $E_{\mathrm{ps,mod}}$ and gravitational potential energy $E_{\mathrm{pg,mod}}$, as given in (19).

[1] S. J. Kim, J. Hasanyan, B. J. Gemmell, S. Lee, and S. Jung, Dynamic criteria of plankton jumping out of water, J. R. Soc. Interface **12**, 20150582 (2015).

[2] B. Chang, J. Myeong, E. Virot, C. Clanet, H.-Y. Kim, and S. Jung, Jumping dynamics of aquatic animals, J. R. Soc. Interface **16**, 20190014 (2019).

[3] B. J. Gemmell, H. Jiang, J. R. Strickler, and E. J. Buskey, Plankton reach new heights in effort to avoid predators, Proc. R. Soc. B **279**, 2786 (2012).

[4] T. T. Truscott, B. P. Epps, and R. H. Munns, Water exit dynamics of buoyant spheres, Phys. Rev. Fluids **1**, 074501 (2016).

[5] J. Rodríguez-Rodríguez, A. Casado-Chacón, and D. Fuster, Physics of beer tapping, Phys. Rev. Lett. **113**, 214501 (2014).
[6] M. Guémas, A. Sellier, and F. Pigeonneau, Low-Reynolds-number rising of a bubble near a free surface at vanishing Bond number, Phys. Fluids **28**, 063102 (2016).
[7] B. A. Puthenveettil, A. Saha, S. Krishnan, and E. J. Hopfinger, Shape parameters of a floating bubble, Phys. Fluids **30**, 112105 (2018).
[8] L. Champougny, E. Rio, F. Restagno, and B. Scheid, The break-up of free films pulled out of a pure liquid bath, J. Fluid Mech. **811**, 499 (2017).
[9] J. R. Tumbleston, D. Shirvanyants, N. Ermoshkin, R. Janusziewicz, A. R. Johnson, D. Kelly, K. Chen, R. Pinschmidt, J. P. Rolland, A. Ermoshkin, E. T. Samulski, and J. M. DeSimone, Continuous liquid interface production of 3d objects, Science **347**, 1349 (2015).
[10] L. N. Jimenez, C. D. V. Martínez Narváez, and V. Sharma, Capillary breakup and extensional rheology response of food thickener cellulose gum (NaCMC) in salt-free and excess salt solutions, Phys. Fluids **32**, 012113 (2020).
[11] R. Zufferey, A. O. Ancel, A. Farinha, R. Siddall, S. F. Armanini, M. Nasr, R. V. Brahmal, G. Kennedy, and M. Kovac, Consecutive aquatic jump-gliding with water-reactive fuel, Sci. Rob. **4**, eaax7330 (2019).
[12] J. Orszaghova, H. Wolgamot, S. Draper, R. Eatock Taylor, P. H. Taylor, and A. Rafiee, Transverse motion instability of a submerged moored buoy, Proc. R. Soc. A **475**, 20180459 (2019).
[13] K. Takamure and T. Uchiyama, Air–water interface dynamics and energy transition in air of a sphere passed vertically upward through the interface, Exp. Therm. Fluid Sci. **118**, 110167 (2020).
[14] K. Takamure and T. Uchiyama, Energy transition in air of a sphere launched vertically upward in water, Ocean Eng. **207**, 107426 (2020).
[15] K. Takamure and T. Uchiyama, Behavior of a solid sphere launched vertically upwards in water and its interaction with the air–water interface, Ocean Eng. **235**, 109282 (2021).
[16] P. Y. Liju, R. Machane, and A. Cartellier, Surge effect during the water exit of an axisymmetric body traveling normal to a plane interface: Experiments and bem simulation, Exp. Fluids **31**, 241 (2001).
[17] A. S. Geller, S. H. Lee, and L. G. Leal, The creeping motion of a spherical particle normal to a deformable interface, J. Fluid Mech. **169**, 27 (1986).
[18] J. G. Telste, Inviscid flow about a cylinder rising to a free surface, J. Fluid Mech. **182**, 149 (1987).
[19] B. Y. Ni and G. X. Wu, Numerical simulation of water exit of an initially fully submerged buoyant spheroid in an axisymmetric flow, Fluid Dyn. Res. **49**, 045511 (2017).
[20] H. Lamb, On some cases of wave-motion on deep water, Ann. Mat. Pura Appl. **21**, 237 (1913).
[21] E. V. Pyatkina, Small-time expansion of wave motion generated by a submerged sphere, J. Appl. Mech. Tech. Phys. **44**, 32 (2003).
[22] R. M. Pardo and J. Nedić, Free-surface disturbances due to the submersion of a cylindrical obstacle, J. Fluid Mech. **926**, A1 (2021).
[23] L. Landau and B. Levich, Dragging of a liquid by a moving plate, Acta Physicochim. USSR. **17**, 42 (1942).
[24] D. Quéré, Fluid coating on a fiber, Annu. Rev. Fluid Mech. **31**, 347 (1999).
[25] E. Rio and F. Boulogne, Withdrawing a solid from a bath: How much liquid is coated? Adv. Colloid Interface Sci. **247**, 100 (2017).
[26] F. Gallaire and P.-T. Brun, Fluid dynamic instabilities: Theory and application to pattern forming in complex media, Philos. Trans. R. Soc. A **375**, 20160155 (2017).
[27] P. M. Reis, S. Jung, J. M. Aristoff, and R. Stocker, How cats lap: Water uptake by felis catus, Science **330**, 1231 (2010).
[28] H. Hao, J. Yu, Y. Song, F. Chen, and T. Liu, Deformation and regimes of liquid column during water exit of a partially submerged sphere using the front-tracking lattice boltzmann method, J. Fluids Struct. **99**, 103152 (2020).
[29] S. J. Kim, S. Kim, and S. Jung, Extremes of the pinch-off location and time in a liquid column by an accelerating solid sphere, Phys. Rev. Fluids **3**, 084001 (2018).
[30] L. Vincent, L. Duchemin, and E. Villermaux, Remnants from fast liquid withdrawal, Phys. Fluids **26**, 031701 (2014).

[31] X. Wei, J. Rivero-Rodríguez, J. Zou, and B. Scheid, Statics and dynamics of a viscous ligament drawn out of a pure-liquid bath, J. Fluid Mech. **922**, A14 (2021).
[32] P. Marmottant and E. Villermaux, Fragmentation of stretched liquid ligaments, Phys. Fluids **16**, 2732 (2004).
[33] J.-L. Pierson and J. Magnaudet, Inertial settling of a sphere through an interface. Part 1. From sphere flotation to wake fragmentation, J. Fluid Mech. **835**, 762 (2018).
[34] X. Zhang, R. S. Padgett, and O. A. Basaran, Nonlinear deformation and breakup of stretching liquid bridges, J. Fluid Mech. **329**, 207 (1996).
[35] J. Zhuang and Y. S. Ju, A combined experimental and numerical modeling study of the deformation and rupture of axisymmetric liquid bridges under coaxial stretching, Langmuir **31**, 10173 (2015).
[36] J. Rivero-Rodríguez, M. Pérez-Saborid, and B. Scheid, An alternative choice of the boundary condition for the arbitrary Lagrangian-Eulerian method, J. Comput. Phys. **443**, 110494 (2021).
[37] X. Wei, W. Wang, F. Lin, B. Scheid, and J. Zou, Delayed bubble entrapment during the drop impact on a bounded liquid bath, AIP Adv. **9**, 105108 (2019).
[38] J. Eggers, Drop formation—An overview, Z. Angew. Math. Mech. **85**, 400 (2005).
[39] Y. Li and J. E. Sprittles, Capillary breakup of a liquid bridge: Identifying regimes and transitions, J. Fluid Mech. **797**, 29 (2016).
[40] R. F. Day, E. J. Hinch, and J. R. Lister, Self-similar capillary pinchoff of an inviscid fluid, Phys. Rev. Lett. **80**, 704 (1998).
[41] A. Deblais, M. A. Herrada, I. Hauner, K. P. Velikov, T. van Roon, H. Kellay, J. Eggers, and D. Bonn, Viscous effects on inertial drop formation, Phys. Rev. Lett. **121**, 254501 (2018).
[42] O. E. Yildirim and O. A. Basaran, Deformation and breakup of stretching bridges of Newtonian and shear-thinning liquids: Comparison of one- and two-dimensional models, Chem. Eng. Sci. **56**, 211 (2001).
[43] J. Eggers and E. Villermaux, Physics of liquid jets, Rep. Prog. Phys. **71**, 036601 (2008).
[44] B. Ni, A. Zhang, and G. Wu, Simulation of complete water exit of a fully-submerged body, J. Fluids Struct. **58**, 79 (2015).
[45] L. Duchemin, S. Le Dizès, L. Vincent, and E. Villermaux, Self-similar impulsive capillary waves on a ligament, Phys. Fluids **27**, 051704 (2015).
[46] M. Tabata and K. Itakura, A precise computation of drag coefficients of a sphere, Int. J. Comput. Fluid Dyn. **9**, 303 (1998).